Materials Science & Engineering A 789 (2020) 139690

Contents lists available at ScienceDirect

Materials Science & Engineering A

journal homepage: www.elsevier.com/locate/msea

Mechanical properties and fracture behavior of Mg–3Al–1Zn alloy under high strain rate loading

Z.H. Dai [a], L. Lu [a,c,*], H.W. Chai [b,**], X.H. Xiao [d], X.L. Gong [c], S.N. Luo [a]

[a] Key Laboratory of Advanced Technologies of Materials, Ministry of Education, and Institute of Material Dynamics, Southwest Jiaotong University, Chengdu, Sichuan 610031, PR China
[b] The Peac Institute of Multiscale Sciences, Chengdu, Sichuan 610031, PR China
[c] CAS Key Laboratory of Mechanical Behavior and Design of Materials, Department of Modern Mechanics, University of Science and Technology of China, Hefei, Anhui 230027, PR China
[d] Advanced Photon Source, Argonne National Laboratory, Argonne, IL 60439, USA

ARTICLE INFO

Keywords:
Magnesium alloys
Mechanical properties
Deformation
Damage

ABSTRACT

Gas-gun experiments are carried out to study the mechanical properties and fracture behavior of a textured Mg–3Al–1Zn alloy under high strain rate. The impact direction (ID) is either perpendicular or parallel to crystallographic {0001} planes, referred to as ID ∥ ⟨c⟩ and ID⊥⟨c⟩, respectively. Shock compression and spallation are achieved with different specimen-to-flyer plate thickness ratios. The Hugoniot elastic limits and spall strengths are estimated as 0.32–0.35 GPa and 0.9–0.92 GPa, respectively, showing weak anisotropy. The deformed specimens are characterized with scanning electron microscope and X-ray computed tomography. Abundant $\{10\bar{1}2\}$ extension twins are activated and the strain hardening rate exhibits a sharp increase and then decrease for the ID⊥⟨c⟩ specimen, while a small number of twins are observed and the hardening rate decreases monotonically for the ID ∥ ⟨c⟩ specimen. As a result of the anisotropic distribution of the β-$Mg_{17}Al_{12}$ phase, cracks are generally distributed in the mid-part and connected together for the ID⊥⟨c⟩ case, while the distribution of cracks in the ID ∥ ⟨c⟩ specimen is relatively discrete along the ID and parallel to the rolling plane.

1. Introduction

Magnesium alloys, as the lightest structural metals, offer a remarkable potential for improving energy efficiency across the automobile and aircraft industries [1–3]. In service, certain structural components are inevitably subjected to dynamic stress. However, magnesium alloys generally exhibit poor ductility at room temperature, restricting their extensive utilization [4,5]. Such a deficiency arises from limited independent deformation modes due to magnesium having hexagonal close-packed (HCP) structure and development of strong basal texture during rolling, which giving rise to anisotropic deformation behaviors [6–8]. Consequently, understanding the anisotropic response of magnesium alloys under dynamic stimuli is of interest, and constructive for a better design and usage of them.

Anisotropic deformation is characteristic of textured magnesium alloys under quasi-static and Kolsky bar loading [8–15]. The stress and hardening rate versus strain relationships in a wide range of strain rate (10^{-3} – 10^{3} s^{-1}) show drastic differences for different loading directions. For quasi-static loading, deformation twinning is considerably inhibited upon compression parallel to the c-axis fibers, while compression perpendicular to c-axis fibers induces the widely-observed $\{10\bar{1}2\}$ extension twinning mode [8]. Furthermore, in cases where massive $\{10\bar{1}2\}$ extension twins are formed, there is an unusual change of concavity with a merging of a regime characterized by an increasing strain hardening rate, known as regime II [16–18]. In Kolsky bar tests, though similar regime II is observed, moderate $\{10\bar{1}1\}$ contraction twins are activated when compressed along c-axis fibers [19].

The Hugoniot elastic limit (HEL) and spall strength of magnesium alloys under plate impact (~10^5 s^{-1} or higher) are extensively investigated [20–25]. Whether the mechanical behavior of magnesium alloys at higher strain rates as in plate impact exhibits an increase in strain hardening rate (regime II) is unclear. Recently, *in situ* X-ray diffraction diagnostics along with molecular dynamics simulations were performed to reveal the deformation of single-crystal magnesium under plate impact, and demonstrated that the dislocation-twinning deformation

* Corresponding author at: Key Laboratory of Advanced Technologies of Materials, Ministry of Education, and Institute of Material Dynamics, Southwest Jiaotong University, Chengdu, Sichuan 610031, PR China.
** Corresponding author.
E-mail addresses: llu@swjtu.edu.cn (L. Lu), hwchai@pims.ac.cn (H.W. Chai).

https://doi.org/10.1016/j.msea.2020.139690
Received 1 April 2020; Received in revised form 24 May 2020; Accepted 31 May 2020
Available online 2 June 2020

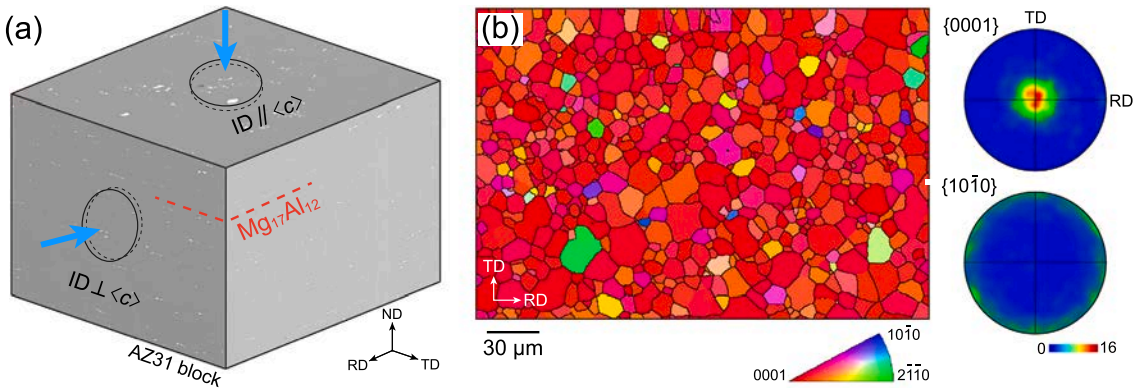

Fig. 1. (a) Pseudo three-dimensional microstructure of the initial Mg–3Al–1Zn alloy block containing the β-$Mg_{17}Al_{12}$ phase (white speckles), and illustration of the relative orientation of the impact direction (ID) with respect to the c-axis fibers. Two types of specimens are prepared. Red dashed lines: distribution of the β-$Mg_{17}Al_{12}$ phase. Black circles: disk-shaped specimens. Blue arrows: impact direction. RD: rolling direction; TD: transverse direction; ND: normal direction. (b) Inverse pole figure map and pole figures of the initial Mg–3Al–1Zn alloy.

mechanisms at a higher strain rate are similar to those of quasi-static and Kolsky bar loading at low and medium strain rates [26]. It is worth investigating whether such deformation mechanisms of single-crystal magnesium can be generalized to polycrystalline magnesium alloys under plate impact.

Since magnesium alloys may be subjected to shock loading during service, their dynamic damage features are also explored in addition to deformation [27–30]. For cast magnesium alloy AZ91, the interface of matrix and strengthening intermetallic phases (β-$Mg_{17}Al_{12}$) is found to act as the crack initiation site under Kolsky bar loading [31], and deformation twinning is also significantly affected by the β-$Mg_{17}Al_{12}$ phase under plate impact [32]. Moreover, microvoids coalescence along the grain boundaries lead to brittle damage inside the as-received wrought Mg–3Al–1Zn alloy, while the damage morphology of specimen treated with equal channel angular pressing is dominated by coalescence of microvoids with inner dimples, indicating ductile fracture [33]. The effects of basal texture and strengthening intermetallic phases on damage features of wrought magnesium alloy are rarely studied.

In this work, we explore mechanical properties and fracture behavior of Mg–3Al–1Zn alloy by gas-gun loading, investigating both shock compression-induced deformation and spallation. The stress–strain curves under high strain rate are derived from free-surface particle velocity. The HEL, yield stress and fracture strength are obtained. The microstructure and damage morphology of deformed specimens are analysed with scanning electron microscopy (SEM) and X-ray computed tomography (XCT). The deformation mechanisms and damage features of specimens shocked along different directions exhibit considerable differences.

2. Materials and experiments

A textured Mg–3Al–1Zn alloy sheet (3 wt% Al, 1 wt% Zn, and balance Mg) containing HCP magnesium and body-centered cubic β-$Mg_{17}Al_{12}$ phases, is used for harvesting specimens for planar impact experiments. Fig. 1a presents its pseudo three-dimensional SEM image. The β-$Mg_{17}Al_{12}$ phase (white speckles) is distributed discretely and located in a plane approximately perpendicular to the normal direction (ND). Inverse pole figure and pole figure maps of the initial Mg–3Al–1Zn specimen obtained from electron back-scatter diffraction (EBSD) analysis are shown in Fig. 1b. The average grain size is about 30 μm. Strong basal fiber texture dominates the Mg–3Al–1Zn alloy: the c-axes, $\langle c\rangle$, is closely aligned with ND. In the following discussion, we take ND as $\langle c\rangle$.

At ambient conditions, the transverse C_T sound velocities along different directions are approximately the same, being 3.10 km s^{-1}, while the longitudinal (C_L) sound velocities parallel and perpendicular to ND determined from ultrasonic measurements are close (5.84 km s^{-1} versus 5.78 km s^{-1}). The average bulk sound velocity C_B is 4.67 km s^{-1}, and the Poisson's ratio ν = 0.33. The density (ρ_0) of Mg–3Al–1Zn alloy is measured as 1.76 g cm^{-3}.

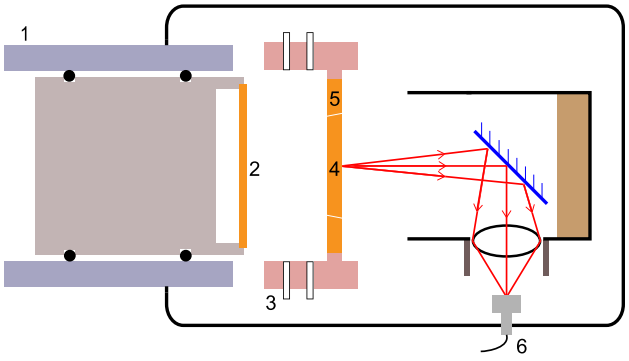

Fig. 2. Experimental setup for gas-gun loading. 1: gun barrel; 2: flyer plate; 3: velocity-measuring system; 4: specimen; 5: momentum trap ring; 6: Doppler pin system (DPS) measuring free-surface velocity.

The experimental setup for shock loading is shown in Fig. 2. A gas gun with a bore diameter of 14 mm is used. High-pressure gas drives a flyer plate (2) to impact the specimen (4). A momentum trap ring (5) around the target, made of the same material as specimen, is placed to weaken the lateral release effect. The impact velocity is measured with a velocity-measuring system (3), and the free-surface particle velocity of the specimen, with DPS (6). The deformed specimens are collected for microstructure characterizations.

Two kinds of specimen-to-flyer plate thickness ratios are prepared to achieve shock compression and spallation experiments. Both the flyer plates and specimens are disk-shaped, and the thicknesses of flyer plates and specimens are 0.75 mm and 1.5 mm for the spallation cases, and 3 mm and 2 mm for the shock compression cases. The diameter of flyer plates (13.5 mm) is larger than the diameter of specimens (9 mm). Given the fiber texture of Mg–3Al–1Zn alloy, two types of specimens (Fig. 1a) are prepared for both the shock compression and spallation cases: the impact direction (ID) is either perpendicular or parallel to the c-axes fibers, referred to as ID ∥ $\langle c\rangle$ and ID⊥$\langle c\rangle$, respectively.

The deformed specimens recovered from shock compression and sectioned with electrical discharge machining to reveal microstructure evolution. For microstructural characterization, the as-received and deformed specimens are mechanically polished with 1000-grit and 2000-grit sandpapers, and then electro-polished in a solution of ethyl alcohol (95%) and perchloric acid (5%) at 5 volts, with a copper rod

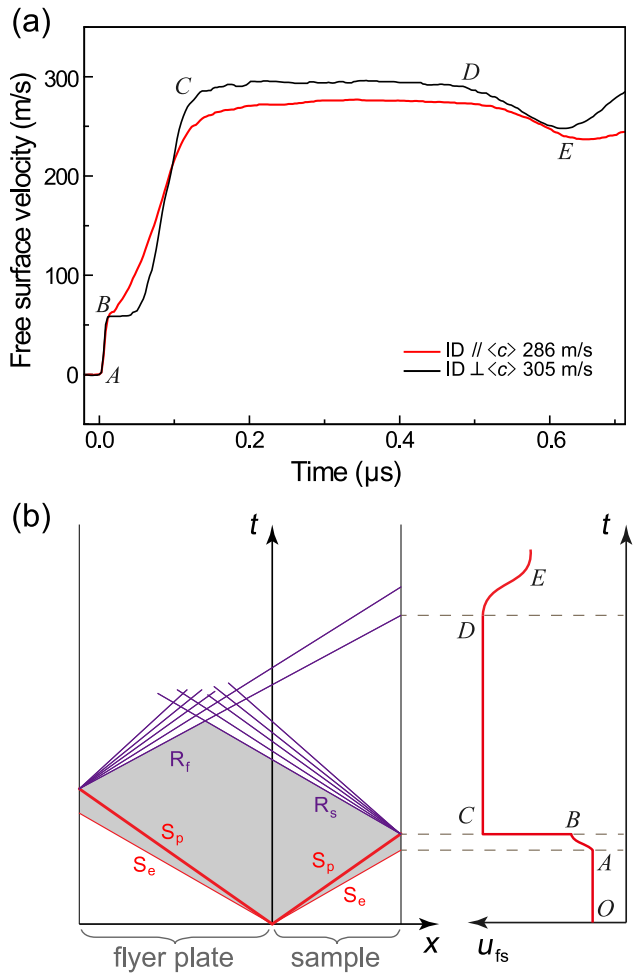

Fig. 3. (a) Free-surface velocity histories of the ID ∥ ⟨c⟩ and ID⊥⟨c⟩ specimens for the shock compression cases. (b) Schematic $x-t$ diagram of wave propagation and corresponding free-surface velocity profile. S_e and S_p represent elastic and plastic shock waves, respectively. R_f and R_s denote release fans.

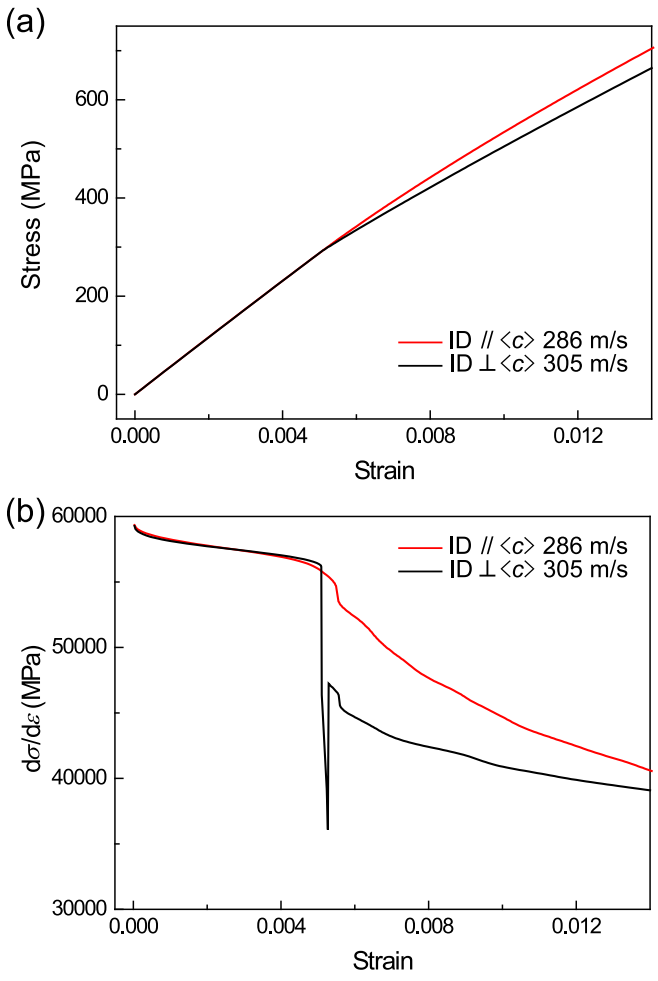

Fig. 4. (a) Stress–strain curves, and (b) strain hardening rate versus strain curves of the ID ∥ ⟨c⟩ and ID⊥⟨c⟩ specimens under planar impact (corresponding to Fig. 3a).

and the sample as electrodes. EBSD characterization as well as SEM analysis, is performed in a field emission gun SEM (FEI Quanta 250 FEG-SEM) equipped with an Oxford EBSD detector. EBSD scanning is conducted at 25 kV, a 15-mm working distance, and a 70° tilt.

Furthermore, XCT is performed to investigate void and crack distributions in the deformed specimens recovered from spallation shots at the 2-BM beamline of the Advanced Photon Source. The imaging specimen is placed in the beam path and the X-ray intensity profiles on the detector (also called projections) are acquired by rotating the specimen during X-ray exposure. The projections for each tomography scan comprise 1500 radiographs in 0° – 180°, which are then reconstructed into volume data using an open-source program TomoPy [34]. The X-ray energy is set at 24.9 keV, and the sample-to-scintillator distance, at 60 mm. The nominal spatial resolution is 0.87 μm per pixel. Similar experimental details were presented elsewhere [35–37].

3. Results and discussion

3.1. Anisotropic deformation: shock compression

The free-surface velocity (u_{fs}) histories of ID ∥ ⟨c⟩ and ID⊥⟨c⟩ specimens for the shock compression cases and schematic diagram of wave propagation along with free-surface velocity profile are shown in Fig. 3. At the moment of impact (O in Fig. 3b), shock waves form and spreed toward the free surfaces of specimen and flyer plate, and are then reflected as release fans on the free surfaces. The region enclosed by shock waves and release fans (gray area in Fig. 3b) undergoes shock compression.

Both the ID ∥ ⟨c⟩ and ID⊥⟨c⟩ specimens exhibit clearly elastic (AB) and plastic (BC) shock waves. Their HEL values, $\sigma_{HEL} = \frac{1}{2}\rho_0 C_L u_{fs}\big|_{HEL}$ [38], are similar (0.32 GPa). Here $u_{fs}\big|_{HEL}$ is the free-surface velocity at point B. The yield stress is 0.16 GPa, as calculated from $\sigma_y = \sigma_{HEL}(1-2\nu)/(1-\nu)$. Nevertheless, the plastic deformation displays significant differences between the ID ∥ ⟨c⟩ and ID⊥⟨c⟩ specimens. The stress–strain curves of textured magnesium alloys at lower strain rates (Kolsky bar and quasi-static loading) show obvious anisotropy when loaded along different directions [17]. For comparison, the free-surface velocity histories are transformed into stress–strain curves according to the Rankine–Hugoniot jump conditions.

For weak shocks, the particle velocity can be approximated as half of the free surface particle velocity. For one-dimensional strain condition, stress σ_i and strain ε_i across the wave front can be obtained from

$$\sigma_i = \sigma_{i-1} + \frac{1}{2}\rho_0 C_i (u_{fs,i} - u_{fs,i-1}), \tag{1}$$

$$\varepsilon_i = \varepsilon_{i-1} + \frac{u_{fs,i} - u_{fs,i-1}}{2C_i}, \tag{2}$$

where subscript $i = 1, 2, 3, \ldots$ represents different moments; $u_{fs,i}$ and C_i denote free-surface velocity and shock wave velocity at moment

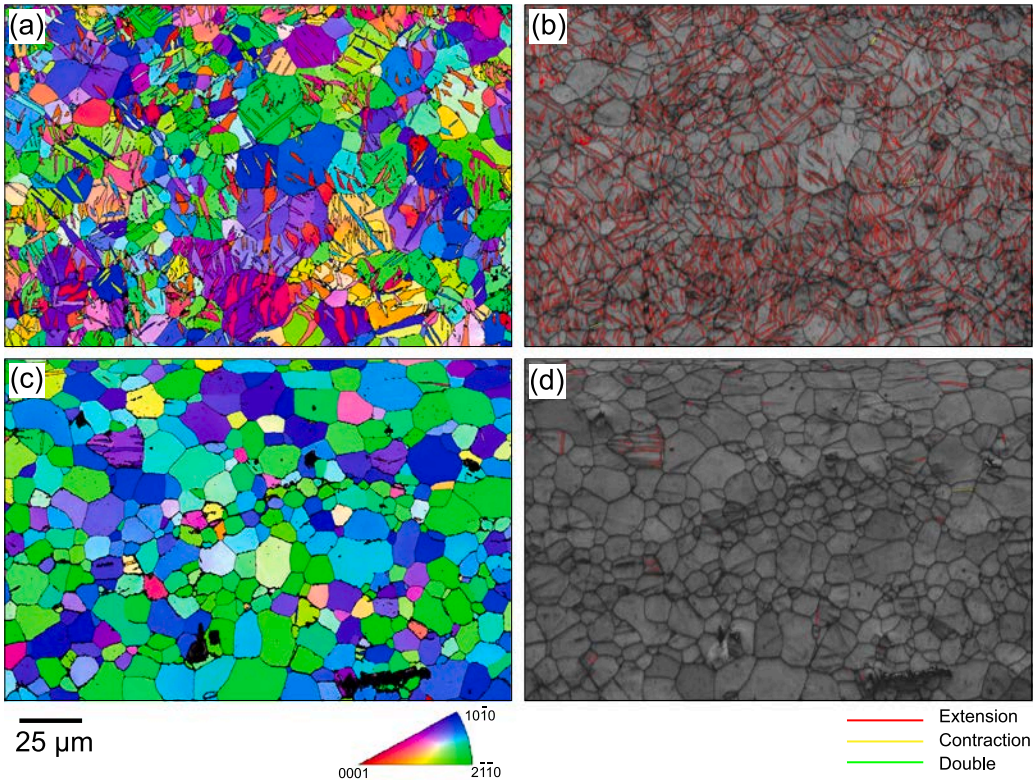

Fig. 5. Microstructure characterization of the specimens recovered from the shock compression cases. (a) and (b) ID⊥⟨c⟩ (impact velocity 305 m/s). (c) and (d) ID ∥ ⟨c⟩ (impact velocity 286 m/s).

i, respectively; and C_i can be calculated with the longitudinal sound velocity (C_L) and the time (τ) for shock wave to arrive at the free surface:

$$C_i = \frac{\delta}{\tau} = \frac{\delta}{\delta/C_L + t_i - t_0}. \quad (3)$$

Here δ is specimen thickness. Given the initial values $\sigma_0 = 0$, $\varepsilon_0 = 0$, $u_{fs,0} = 0$, and $t_0 = 0$, and the current values $u_{fs,1}$ and t_1 in Fig. 3(a), substituting Eq. (3) into Eqs. (1) and (2) yields σ_1 and ε_1. By repeating this process, all σ_i and ε_i can be calculated.

Fig. 4a presents the stress–strain curves for the ID ∥ ⟨c⟩ and ID⊥⟨c⟩ specimens. They coincide in the elastic stage but deviate in the plastic stage. The corresponding strain hardening rates ($d\sigma/d\varepsilon$, derived from the stress–strain curves) are also calculated (Fig. 4b). After yield, the strain hardening rate reduces drastically. Thereafter, the rate decreases for the ID ∥ ⟨c⟩ specimen, but undergoes a sharp growth followed by gradual reduction for the ID⊥⟨c⟩ specimen. These features of the strain hardening rate curves for plate impact are similar to those achieved under quasi-static and Kolsky bar loading; the deformation of the magnesium alloy at higher strain rates (~2×10^5 s^{-1}) demonstrates three regimes for the ID⊥⟨c⟩ loading, similar to the experiments at lower strain rates (10^{-3}–10^3 s^{-1}) [17,19].

EBSD characterizations of the recovered ID ∥ ⟨c⟩ and ID⊥⟨c⟩ specimens are presented in Fig. 5. The EBSD maps show abundant $\{10\bar{1}2\}$ extension twins in the ID⊥⟨c⟩ specimen, while a small number of $\{10\bar{1}2\}$ extension twins are observed in the ID ∥ ⟨c⟩ case, and few $\{10\bar{1}1\}$ contraction twins are formed in both cases.

For planar impact, the extension twinning occurs upon shock compression along $\langle 11\bar{2}0\rangle$ and $\langle 10\bar{1}0\rangle$, but only upon release for loading along ⟨0001⟩ in single crystal magnesium, as demonstrated with ultrafast synchrotron X-ray diffraction [26]. It can be inferred that numerous $\{10\bar{1}2\}$ extension twins are activated during shock compression (BC in Fig. 3a) in the ID⊥⟨c⟩ case. Once deformation twins nucleate within grains, they grow rapidly; twin boundaries are planar and efficient in sweeping across a sample area. Thus, the strain gradients can be released by twinning to achieve strain delocalization, effectively boosting strain hardening rate in the ID⊥⟨c⟩ specimen (Fig. 4). In addition, the increase in strain hardening rate may be related to a transition from initial basal slip to non-basal slip, caused by the penetration of basal slip between slightly disoriented grains, whereby an enhanced resolved basal strength arises (with respect to single crystals) [39]. Nevertheless, dislocation motion dominates the plastic deformation of the ID ∥ ⟨c⟩ specimen rather than deformation twinning during shock compression. Owing to short slide length and pileup, dislocations nucleated at defects such as grain boundaries induce strain localization, leading to slight decrease in strain hardening rate. Overall, the macroscale mechanical properties of magnesium alloy exhibit anisotropy (Figs. 3 and 4). In other words, the stress–strain curve features and microstructure of Mg–3Al–1Zn alloy under plate impact are similar to those under quasi-static or Kolsky bar cases, independent of strain rate.

3.2. Anisotropic damage: spallation

For spallation (shock-induced tension) experiments, the specimen-flyer plate thickness ratio is increased to 2:1. Fig. 6a shows the free-surface velocity histories of ID ∥ ⟨c⟩ and ID⊥⟨c⟩ specimens. The principle of spallation is illustrated with a schematic diagram of wave propagation with corresponding free-surface velocity profile (Fig. 6b). Similar to the shock compression cases, elastic and plastic shock waves form and propagate toward the free surfaces after impact, resulting in increases in free-surface velocity(AC). The arrival of the release fan reflected from the free surface of the flyer plate reduces the velocity (DE). Unlike shock compression cases, the subsequent interaction of release fans occurs in the mid-part of specimen (R_s in Fig. 6b) and changes the stress from compression to tension. When the tension stress exceeds the dynamic fracture strength, termed as the spall strength σ_{sp}, spallation occurs. In the meantime, a compression wave forms in the

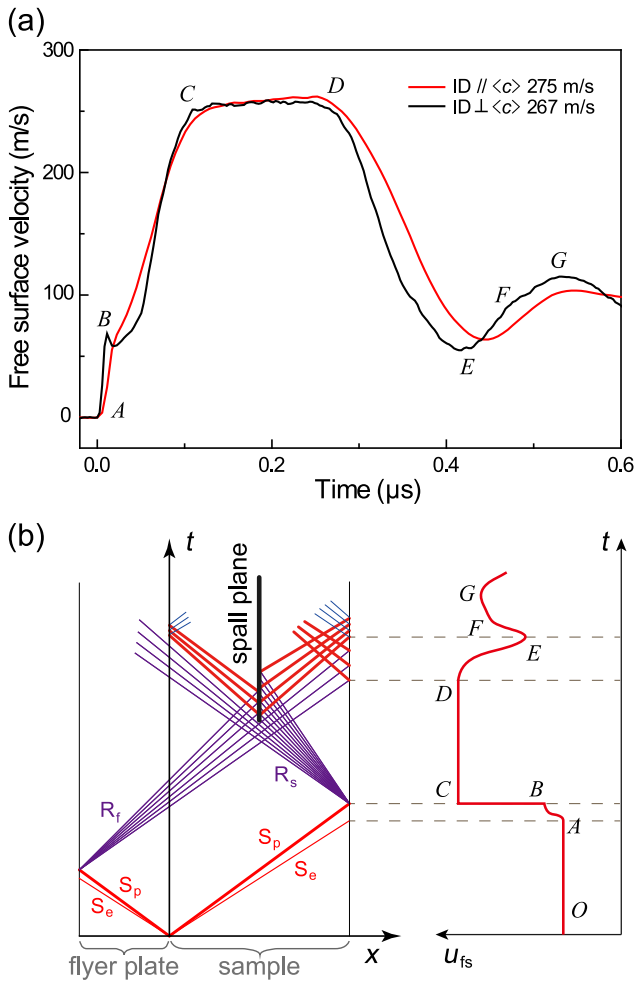

Fig. 6. (a) Free-surface velocity histories of the ID ∥ ⟨c⟩ and ID⊥⟨c⟩ specimens for the spallation cases. (b) Schematic $x-t$ diagram of wave propagation and corresponding free-surface velocity profile.

damage region (spall plane in Fig. 6b) and propagate toward the free surface, resulting in the increase of free-surface velocity history (EF).

The HEL values for the ID ∥ ⟨c⟩ and ID⊥⟨c⟩ loading are 0.34 and 0.35 GPa, respectively, similar to those obtained in the shock compression cases. The slope of segment DE can be utilized to estimate the tensile strain rate with $\dot{\varepsilon} \approx [\mathrm{d}u_{fs}(t)/\mathrm{d}t]|_{DE}/(2C_L)$, and the tensile strain rates for the ID ∥ ⟨c⟩ and ID⊥⟨c⟩ loading are 1.0×10^5 s^{-1} and 1.2×10^5 s^{-1}, respectively.

Different from the fracture strength under quasi-static or Kolsky bar loading, which can be measured with a stress or strain gauge, the fracture strength for plate impact is generally estimated as $\sigma_{sp} \approx \rho_0(u_{fs}|_D - u_{fs}|_E)C_L C_B/(C_L + C_B)$. The spall strength of the ID ∥ ⟨c⟩ specimen, ~0.90 GPa, is slightly less than that of the ID⊥⟨c⟩ specimen, 0.92 GPa. According to the shock compression results, massive $\{10\bar{1}2\}$ extension twins are formed during shock compression (BC in Fig. 4a) in the ID⊥⟨c⟩ specimen. During dynamic tension (DE), the already formed twins can contribute to strain hardening by texture hardening, and twin–twin and dislocation–twin interactions [40,41]. In addition, the deformation twins can act as nucleation sites of microcracks, reducing fracture strength [42,43]. Moreover, spall strength of a metal generally increases with increasing strain rate [43,44]. The slightly higher spall strength in the ID⊥⟨c⟩ specimen may be attributed to the higher strain rate.

XCT characterization is performed on the recovered ID ∥ ⟨c⟩ and ID⊥⟨c⟩ specimens recovered from the spallation shots to explore the distributions of voids and cracks (Fig. 7). Consistent with the SEM characterization (Fig. 1a), the β-$Mg_{17}Al_{12}$ phase is roughly distributed along the RD–TD plane. For the ID⊥⟨c⟩ specimen, cracks are generally distributed in the mid-part and connected together, while the distribution of cracks in the ID ∥ ⟨c⟩ specimen is relatively discrete along the impact direction and parallel to the RD–TD plane. Cracks are prone to nucleate at the Mg/$Mg_{17}Al_{12}$ interfaces under high strain rate loading [32]. The significant difference in damage morphology between the ID ∥ ⟨c⟩ and ID⊥⟨c⟩ specimens described above can be ascribed to the anisotropic distribution of β-$Mg_{17}Al_{12}$ phases.

For the ID ∥ ⟨c⟩ loading, the small patches of the β-$Mg_{17}Al_{12}$ phase serving as the weak zones for damage nucleation are located on the RD–TD plane, which is perpendicular to the direction of maximum tensile stress (impact direction). As a consequence, in addition to the middle principal crack, the cracks can also be formed in regions with less tensile stress (weak zones, parallel to the RD–TD plane) near the principal crack. While the small cracks near the spall plane are difficult to grow and coalesce along the direction perpendicular to the maximum tensile stress for the ID⊥⟨c⟩ loading, due to the weak zones (RD–TD plane) parallel to the impact direction, and a large principal crack is formed and located in the mid-part of the recovered specimen. The damage degree, defined as the ratio of the damaged volume to the whole volume under consideration, is calculated. The damage degree for the ID⊥⟨c⟩ specimen is 1.03%, and is less than that of the ID ∥ ⟨c⟩ specimen (1.23%).

Fig. 8 exhibits the quantitative relationships between the number and size of voids and cracks for the ID ∥ ⟨c⟩ and ID⊥⟨c⟩ spallation specimens. Because of the large volume range of voids and cracks, their numbers are counted at seven volume ranges, 10^0–10^1, 10^1–10^2, 10^2–10^3, 10^3–10^4, 10^4–10^5, 10^5–10^6, and 10^6–10^7 μm^3 (marked with different colors in Fig. 8), in order to clearly exhibit the number–size distribution; their binning sizes are 9, 10, 10^2, 10^3, 10^4, 10^5, 10^6 μm^3, respectively. The number of small voids/cracks (below 100 μm^3) in the ID⊥⟨c⟩ specimen is larger than the number of the ID ∥ ⟨c⟩ specimen. When the void/crack volume exceeds 100 μm^3, the number of voids/cracks in the ID ∥ ⟨c⟩ specimen is more than that in the ID⊥⟨c⟩ specimen. Such differences may be due to the weak zones parallel to the spall plane in the ID ∥ ⟨c⟩ specimen which are favorable for void growth and coalescence of isolated crack/void, and thus reduce the number of small voids and cracks (<100 μm^3) and increase the number of larger voids/cracks. Furthermore, as marked with the arrow in Fig. 8, the volume of the principal crack for the ID⊥⟨c⟩ specimen is the largest, which is several times the volume of the largest crack in the ID ∥ ⟨c⟩ specimen.

In addition, the closest distance between a void/crack and neighboring β-$Mg_{17}Al_{12}$ phase, is calculated for both specimens, and the average distances for each volume range are shown in Fig. 9. As the volume of void/crack increases, the average distance as well as the standard deviation decreases for both ID ∥ ⟨c⟩ and ID⊥⟨c⟩ specimens. When the volume of void/crack is relatively low (<60 μm^3), the average distances at each volume range for both specimens are approximately equal (about 10 μm), and the large standard deviations demonstrate that the void/crack can form at phase boundaries as well as the grain boundaries away from the β-$Mg_{17}Al_{12}$ phase. For larger void/crack volumes, the average distances for the ID ∥ ⟨c⟩ specimen are less than those of the ID⊥⟨c⟩ specimen, indicating that the β-$Mg_{17}Al_{12}$ phase is more conducive to the growth and coalescence of void/crack in the ID ∥ ⟨c⟩ specimen than ID⊥⟨c⟩ specimen.

Given their limited number of slip systems and high twinning activity, wrought magnesium alloys tend to develop a strong basal texture during manufacture [45]. Consequently, they typically exhibit both tension–compression asymmetry as well as anisotropy under quasi-static and Kolsky bar loading [46–49]. As described above, the responses of the magnesium alloy under both shock compression and tension (spallation) display considerable anisotropy. Nevertheless, tension always occurs after shock compression, and shock compression and

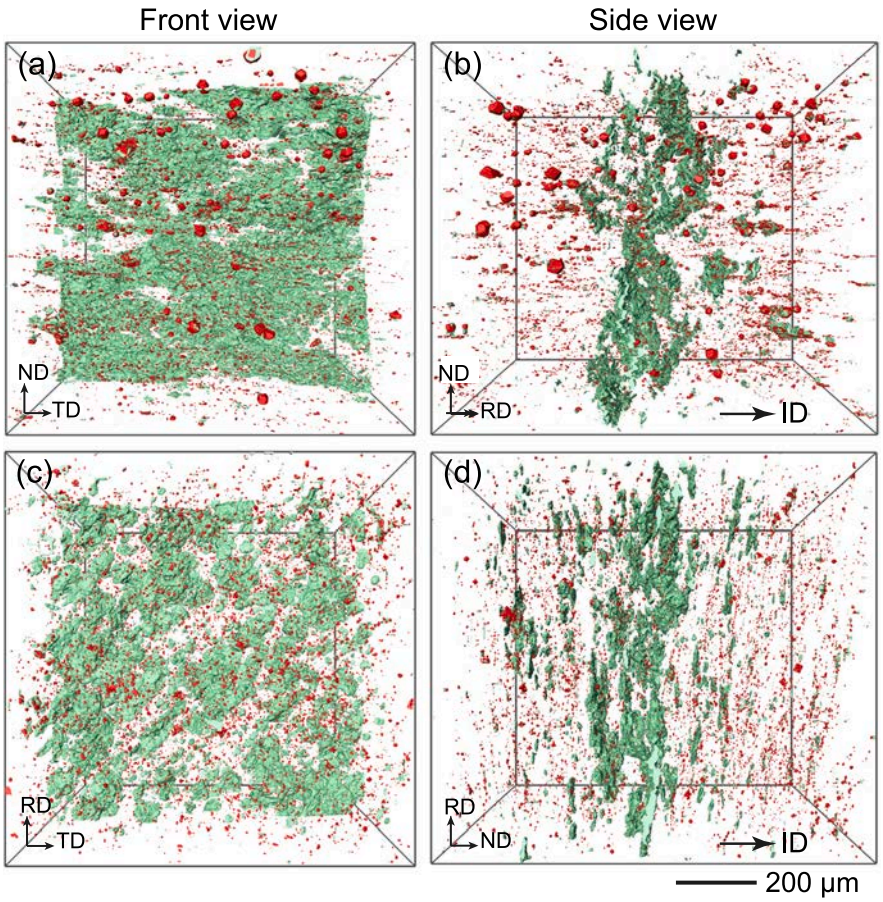

Fig. 7. X-ray computed tomography images of the specimens recovered form the spallation cases. (a) and (b) ID⊥⟨c⟩. (c) and (d) ID ∥ ⟨c⟩. Green: voids or cracks; red: the β-$Mg_{17}Al_{12}$ phase. Impact direction (ID) is marked in the right column. The sampling volume is 1100 × 1100 × 1200 μm^3. (For interpretation of the references to color in this figure legend, the reader is referred to the web version of this article.)

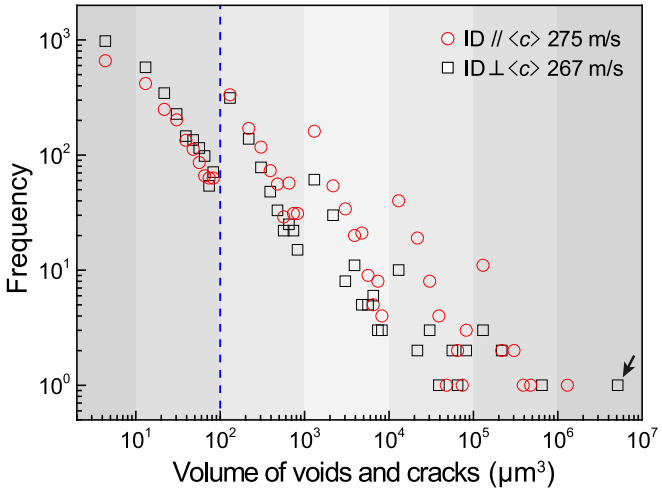

Fig. 8. Quantitative relationships between the number and size of voids and cracks for the ID⊥⟨c⟩ and ID ∥ ⟨c⟩ spallation specimens.

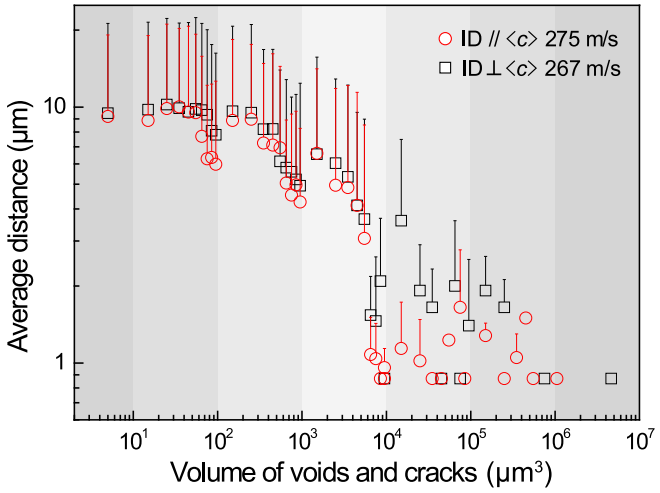

Fig. 9. Number–distance relationships of voids/cracks for the ID⊥⟨c⟩ and ID ∥ ⟨c⟩ spallation specimens.

tension are generally used to investigate deformation and damage, respectively. Therefore, it is difficult to explore the tension–compression asymmetry with plate impact compared to loading with materials testing systems and Kolsky bars. New devices and diagnostic methods are needed for this matter.

4. Summary

Shock compression and spallation experiments are conducted on a rolled Mg–3Al–1Zn alloy along two orientations: ID ∥ ⟨c⟩ and ID⊥⟨c⟩, to explore its mechanical properties and damage, respectively. Free-surface velocity history is obtained to derive stress–strain curves.

Microstructural features of deformed specimens are characterized with EBSD and synchrotron XCT.

The impact responses of the ID ∥ ⟨c⟩ and ID⊥⟨c⟩ specimens show considerable differences. The strain hardening rate for the ID ∥ ⟨c⟩ specimen decreases monotonically, while it exhibits a sharp increase and then decrease for the ID⊥⟨c⟩ specimen. Massive $\{10\bar{1}2\}$ extension twins are activated in the ID⊥⟨c⟩ specimen, while a small number of $\{10\bar{1}2\}$ extension twins are observed for the ID ∥ ⟨c⟩ specimen, and few of $\{10\bar{1}1\}$ contraction twins are formed in both types of specimens.

The spall strength for both cases are similar. Nevertheless, the damage features including morphology are different, as a result of anisotropic distribution of the β-$Mg_{17}Al_{12}$ phase. For the ID⊥⟨c⟩ specimen, cracks are generally distributed in the mid-part and connected together, while the distribution of cracks in the ID ∥ ⟨c⟩ specimen is relatively discrete along the impact direction and parallel to the RD–TD plane.

CRediT authorship contribution statement

Z.H. Dai: Methodology, Investigation, Visualization, Writing - original draft. **L. Lu:** Conceptualization, Data curation, Formal analysis, Writing - review & editing, Funding acquisition. **H.W. Chai:** Methodology, Formal analysis, Visualization. **X.H. Xiao:** Resources. **X.L. Gong:** Validation, Resources. **S.N. Luo:** Writing - review & editing, Validation, Supervision, Funding acquisition, Resources.

Declaration of competing interest

The authors declare that they have no known competing financial interests or personal relationships that could have appeared to influence the work reported in this paper.

Acknowledgments

This work was sponsored in part by the Scientific Challenge Project of China (Grant No. TZ2018001) and the National Natural Science Foundation of China (Grant Nos. 11627901 and 11902274). Use of the Advanced Photon Source, an Office of Science User Facility operated for the U.S. Department of Energy (DOE) Office of Science by Argonne National Laboratory, was supported by the U.S. DOE under Contract No. DE-AC02-06CH11357.

References

[1] T.M. Pollock, Weight loss with magnesium alloys, Science 328 (2010) 986–987.
[2] A. Yamashita, Z. Horita, T.G. Langdon, Improving the mechanical properties of magnesium and a magnesium alloy through severe plastic deformation, Mater. Sci. Eng. A 300 (2001) 142–147.
[3] T. Trang, J. Zhang, J. Kim, A. Zargaran, J. Hwang, B.-C. Suh, N. Kim, Designing a magnesium alloy with high strength and high formability, Nature Commun. 9 (2018) 1–6.
[4] B.-C. Suh, M.-S. Shim, K. Shin, N.J. Kim, Current issues in magnesium sheet alloys: where do we go from here? Scripta Mater. 84 (2014) 1–6.
[5] Z. Wu, R. Ahmad, B. Yin, S. Sandlöbes, W. Curtin, Mechanistic origin and prediction of enhanced ductility in magnesium alloys, Science 359 (2018) 447–452.
[6] S.R. Agnew, Ö. Duygulu, Plastic anisotropy and the role of non-basal slip in magnesium alloy AZ31B, Int. J. Plast. 21 (2005) 1161–1193.
[7] B. Mao, B. Li, D. Lin, Y. Liao, Enhanced room temperature stretch formability of AZ31B magnesium alloy sheet by laser shock peening, Mater. Sci. Eng. A 756 (2019) 219–225.
[8] A.L. Oppedal, H. El Kadiri, C.N. Tomé, G.C. Kaschner, S.C. Vogel, J.C. Baird, M.F. Horstemeyer, Effect of dislocation transmutation on modeling hardening mechanisms by twinning in magnesium, Int. J. Plast. 30 (2012) 41–61.
[9] M.R. Barnett, Z. Keshavarz, A.G. Beer, D. Atwell, Influence of grain size on the compressive deformation of wrought Mg–3Al–1Zn, Acta Mater. 52 (2004) 5093–5103.
[10] N. Stanford, K. Sotoudeh, P.S. Bate, Deformation mechanisms and plastic anisotropy in magnesium alloy AZ31, Acta Mater. 59 (2011) 4866–4874.
[11] B.S. Wang, R.L. Xin, G.J. Huang, Q. Liu, Effect of crystal orientation on the mechanical properties and strain hardening behavior of magnesium alloy AZ31 during uniaxial compression, Mater. Sci. Eng. A 534 (2012) 588–593.
[12] L. Lu, B.X. Bie, Q.H. Li, T. Sun, K. Fezzaa, X.L. Gong, S.N. Luo, Multiscale measurements on temperature-dependent deformation of a textured magnesium alloy with synchrotron x-ray imaging and diffraction, Acta Mater. 132 (2017) 389–394.
[13] M.T. Tucker, M.F. Horstemeyer, P.M. Gullett, H.E. Kadiri, W.R. Whittington, Anisotropic effects on the strain rate dependence of a wrought magnesium alloy, Scripta Mater. 60 (2009) 182–185.
[14] I. Ulacia, N.V. Dudamell, F. Gálvez, S. Yi, M.T. Pérez-Prado, I. Hurtado, Mechanical behavior and microstructural evolution of a Mg AZ31 sheet at dynamic strain rates, Acta Mater. 58 (2010) 2988–2998.
[15] N. Dixit, K.Y. Xie, K.J. Hemker, K.T. Ramesh, Microstructural evolution of pure magnesium under high strain rate loading, Acta Mater. 87 (2015) 56–67.
[16] E. Kelley, W. Hosford, Plane-strain compression of magnesium and magnesium alloy crystals, Trans. Met. Soc. AIME 242 (1968) 5–13.
[17] M. Knezevic, A. Levinson, R. Harris, R.K. Mishra, R.D. Doherty, S.R. Kalidindi, Deformation twinning in AZ31: influence on strain hardening and texture evolution, Acta Mater. 58 (2010) 6230–6242.
[18] L. Lu, J.W. Huang, D. Fan, B.X. Bie, T. Sun, K. Fezzaa, X.L. Gong, S.N. Luo, Anisotropic deformation of extruded magnesium alloy AZ31 under uniaxial compression: A study with simultaneous in situ synchrotron x-ray imaging and diffraction, Acta Mater. 120 (2016) 86–94.
[19] L. Lu, T. Sun, K. Fezzaa, X. Gong, S. Luo, Simultaneous multiscale measurements on dynamic deformation of a magnesium alloy with synchrotron x-ray imaging and diffraction, Mater. Sci. Eng. A 701 (2017) 143–148.
[20] G.I. Kanel, S.V. Razorenov, A. Bogatch, A.V. Utkin, D.E. Grady, Simulation of spall fracture of aluminum and magnesium over a wide range of load duration and temperature, Int. J. Impact Eng. 20 (1997) 467–478.
[21] J.C.F. Millett, S.M. Stirk, N.K. Bourne, G.T. Gray, On the behaviour of the magnesium alloy, AZ61 to one-dimensional shock loading, Acta Mater. 58 (2010) 5675–5682.
[22] G.V. Garkushin, G.I. Kanel, S.V. Razorenov, High strain rate deformation and fracture of the magnesium alloy Ma2-1 under shock wave loading, Phys. Solid State 54 (2012) 1079–1085.
[23] P. Renganathan, J. Winey, Y. Gupta, Shock compression and release of a-axis magnesium single crystals: anisotropy and time dependent inelastic response, J. Appl. Phys. 121 (2017) 035901.
[24] N. Dixit, L. Farbaniec, K. Ramesh, Twinning in single crystal mg under microsecond impact along the ⟨a⟩ axis, Mater. Sci. Eng. A 693 (2017) 22–25.
[25] P.J. Hazell, G.J. Appleby-Thomas, E. Wielewski, C. Stennett, C. Siviour, The influence of microstructure on the shock and spall behaviour of the magnesium alloy, elektron 675, Acta Mater. 60 (2012) 6042–6050.
[26] S. Chen, Y.X. Li, N.B. Zhang, J.W. Huang, H.M. Hou, S.J. Ye, T. Zhong, X.L. Zeng, D. Fan, L. Lu, L. Wang, T. Sun, K. Fezzaa, Y.Y. Zhang, M.X. Tang, S.N. Luo, Capture deformation twinning in Mg during shock compression with ultrafast synchrotron x-ray diffraction, Phys. Rev. Lett. 123 (2019) 255501.
[27] A. Rodriguez, G. Ayoub, B. Mansoor, A. Benzerga, Effect of strain rate and temperature on fracture of magnesium alloy AZ31B, Acta Mater. 112 (2016) 194–208.
[28] K. Tokaji, M. Kamakura, Y. Ishiizumi, N. Hasegawa, Fatigue behaviour and fracture mechanism of a rolled az31 magnesium alloy, Int. J. Fracture 26 (2004) 1217–1224.
[29] Y.Z. Lü, Q.D. Wang, W.J. Ding, X.Q. Zeng, Y.P. Zhu, Fracture behavior of AZ91 magnesium alloy, Mater. Lett. 44 (2000) 265–268.
[30] X. Jin, W. Xu, K. Li, X. Zeng, D. Shan, Influence of heat treatment on the evolution of microstructure and mechanical properties of Mg-7Gd-5Y-0.6Zn-0.8Zr magnesium alloy, Mater. Sci. Eng. A 729 (2018) 219–229.
[31] H. Asgari, J.A. Szpunar, A.G. Odeshi, Texture evolution and dynamic mechanical behavior of cast AZ magnesium alloys under high strain rate compressive loading, Mate. Design 61 (2014) 26–34.
[32] M. Wang, L. Lu, C. Li, X.H. Xiao, X.M. Zhou, J. Zhu, S.N. Luo, Deformation and spallation of a magnesium alloy under high strain rate loading, Mater. Sci. Eng. A 661 (2016) 126–131.
[33] X. Yu, T. Li, L. Li, S. Liu, Y. Li, Influence of initial texture on the shock property and spall behavior of magnesium alloy AZ31B, Mater. Sci. Eng. A 700 (2017) 259–268.
[34] D. Gürsoy, F. De Carlo, X. Xiao, C. Jacobsen, Tomopy: a framework for the analysis of synchrotron tomographic data, J. Synchrotron Radiat. 21 (2014) 1188–1193.
[35] H.W. Chai, H.Y. Li, X.H. Xiao, J.Y. Huang, S.N. Luo, Correlation between cell wall buckling and deformation banding in a closed-cell foam, Scripta Mater. 170 (2019) 177–182.
[36] J. Moosmann, A. Ershov, V. Altapova, T. Baumbach, M.S. Prasad, C. LaBonne, X. Xiao, J. Kashef, R. Hofmann, X-ray phase-contrast in vivo microtomography probes new aspects of Xenopus gastrulation, Nature 497 (2013) 374.

[37] X.C. Tang, C. Li, H.Y. Li, X.H. Xiao, L. Lu, X.H. Yao, S.N. Luo, Cup-cone structure in spallation of bulk metallic glasses, Acta Mater. 178 (2019) 219–227.
[38] M.A. Meyers, Dynamic behavior of materials, John Wiley & Sons, New York, 1994.
[39] J. Balík, P. Dobroň, F. Chmelík, R. Kužel, D. Drozdenko, J. Bohlen, D. Letzig, P. Lukáč, Modeling of the work hardening in magnesium alloy sheets, Int. J. Plast. 76 (2016) 166–185.
[40] J. Zhang, S.P. Joshi, Phenomenological crystal plasticity modeling and detailed micromechanical investigations of pure magnesium, J. Mech. Phys. Solids 60 (2012) 945–972.
[41] A.A. Salem, S. Kalidindi, R. Doherty, S. Semiatin, Strain hardening due to deformation twinning in α-titanium: mechanisms, Metall. Mater. Trans. A 37 (2006) 259–268.
[42] M. Gzyl, R. Pesci, A. Rosochowski, S. Boczkal, L. Olejnik, In situ analysis of the influence of twinning on the strain hardening rate and fracture mechanism in AZ31B magnesium alloy, J. Mater. Sci. 50 (2015) 2532–2543.
[43] C. Li, K. Yang, X.C. Tang, L. Lu, S.N. Luo, Spall strength of a mild carbon steel: Effects of tensile stress history and shock-induced microstructure, Mater. Sci. Eng. A 754 (2019) 461–469.
[44] C. Li, B. Li, J.Y. Huang, H.H. Ma, M.H. Zhu, J. Zhu, S.N. Luo, Spall damage of a mild carbon steel: effects of peak stress, strain rate and pulse duration, Mater. Sci. Eng. A 660 (2016) 139–147.
[45] S.A. Habib, A.S. Khan, T. Gnäupel-Herold, J.T. Lloyd, S.E. Schoenfeld, Anisotropy, tension-compression asymmetry and texture evolution of a rare-earth-containing magnesium alloy sheet, ZEK100, at different strain rates and temperatures: Experiments and modeling, Int. J. Plast. 95 (2017) 163–190.
[46] A. Jain, S.R. Agnew, Modeling the temperature dependent effect of twinning on the behavior of magnesium alloy AZ31B sheet, Mater. Sci. Eng. A 462 (2007) 29–36.
[47] X.Y. Lou, M. Li, R.K. Boger, S.R. Agnew, R.H. Wagoner, Hardening evolution of AZ31B Mg sheet, Int. J. Plast. 23 (2007) 44–86.
[48] J.T. Wang, J.Q. Liu, X. Zhao, et al., On tension−compression yield asymmetry in an extruded Mg-3Al-1Zn alloy, J. Alloys Compd. 478 (2009) 789–795.
[49] S. Kurukuri, M.J. Worswick, D. Ghaffari Tari, R.K. Mishra, J.T. Carter, Rate sensitivity and tension−compression asymmetry in AZ31B magnesium alloy sheet, Philos. T. R. Soc. A 372 (2014) 20130216.